Draft version July 27, 2026
Typeset using LaTeX **twocolumn** style in AASTeX7

https://doi.org/10.71929/rubin/3377440

# The Vera C. Rubin Observatory Data Preview 2

Vera C. Rubin Observatory Team[1]

[1] *NSF-DOE Vera C. Rubin Observatory / NSF NOIRLab, 950 N. Cherry Ave., Tucson, AZ 85719, USA*

(Dated: July 27, 2026)


## ABSTRACT

We present an early version of Rubin Data Preview 2 (DP2), the second data preview from the National Science Foundation–Department of Energy Vera C. Rubin Observatory. Early Data Preview 2 (EDP2) comprises coadds, detection catalogs, and ancillary data products; eventually, the full DP2 will also include single-epoch images and difference images, but any analysis begun on EDP2 will require no modification. DP2 is derived from observations acquired by the LSST Science Camera (LSSTCam) on the Simonyi Survey Telescope at the Summit Facility on Cerro Pachón, Chile, primarily during the on-sky commissioning campaign between 2025-04-16 and 2025-09-21, supplemented by observations taken between 2025-10-25 and 2026-01-06 that overlap the commissioning footprint. The DP2 footprint comprises the Science Validation wide-area survey, five Deep Drilling Fields, and a number of targeted small-field regions, including Trifid and Lagoon, Prawn, M49, and New Horizons, all observed as part of the Rubin First Look campaign. Each field was imaged in up to six broad photometric bands, *ugrizy*, and coadded to produce deep imaging covering an estimated 3,000 deg$^2$. The addition of single-visit-only areas expands the total DP2 footprint to an estimated 15,000 deg$^2$, with coverage in at least one filter. The median per-visit PSF FWHM across the wide-area survey ranges from 1.17 arcsec in the $z$ band to 1.26 arcsec in $g$ and $r$ bands, with the sharpest fields reaching $\sim 0\farcs0$. COSMOS, the deepest field, reaches estimated coadded $5\sigma$ depths of $u$=26 mag, $g$=26.8 mag, $r$=26.3 mag, $i$=26.1 mag, $z$=25.3 mag, $y$=23.9 mag. DP2 contains X distinct astrophysical objects, of which X are extended in at least one band in coadds, and X solar system objects, of which X are new discoveries. DP2 is approximately 59.15 TB in size and is available to Vera C. Rubin Observatory data rights holders via the Rubin Science Platform, a cloud-based environment for the analysis of petascale astronomical data. Based on a roughly five-month primary observing baseline and covering only part of the eventual LSST footprint, DP2's area, depth, and multiband coverage nonetheless support a broad range of early science investigations ahead of LSST Data Release 1.


*Keywords:* Rubin Observatory - LSST

## 1. INTRODUCTION

The National Science Foundation (NSF)–Department of Energy (DOE) Vera C. Rubin Observatory is a ground-based, wide-field optical-near-infrared facility on Cerro Pachón in northern Chile, built to carry out the Legacy Survey of Space and Time (LSST) (Ivezić et al. 2019). The observatory is named in honor of Vera C. Rubin, whose observations in the latter half of the 20th century established the first compelling empirical case for dark matter (Rubin & Ford 1970; Rubin et al. 1980). Its 10-yr survey will image the entire visible southern sky every 3–4 nights, reaching a coadded depth of $\sim 27$ mag in the $r$-band across an 18000 deg$^2$ footprint (Bianco et al. 2022).

At the heart of the facility is the 3.2 gigapixels-gigapixel LSST Science Camera (LSSTCam), mounted on the 8.4 m (6.5 m effective aperture) Simonyi Survey Telescope (Stalder et al. 2024). Together they deliver an instantaneous field of view of 9.6 deg$^2$ in six broadband filters, *ugrizy* (320–1050 nm), with seeing-limited image quality. The system's étendue of 319 deg$^2$ m$^2$ exceeds that of any previous optical facility by over an order of magnitude, enabling the rapid, deep, all-sky cadence that underpins Rubin's four core science themes: the

Corresponding author: Leanne P. Guy, James Mullaney, Alex Broughton

nature of dark energy and dark matter; a census of the solar system; the transient and variable optical sky; and the structure of the Milky Way (Ivezić et al. 2019). An automated Data Management System processes tens of terabytes of images per night to produce science-ready data products within minutes of each observation for a global community of scientists.

This paper presents Rubin's third Data Preview, Data Preview 2 (DP2) (NSF-DOE Vera C. Rubin Observatory 2025), and the first to be based entirely on LSSTCam data. It marks the conclusion of the Rubin commissioning program and the transition to full survey operations. DP2 is a reprocessing of all science-grade exposures acquired with LSSTCam during on-sky commissioning and the initial phase of early operations, prior to the formal start of the LSST on 2026-06-29. As such, it represents a natural boundary and provides a comprehensive dataset that captures the on-sky performance of the as-built system at the end of the Rubin construction project.

Two earlier Data Previews preceded DP2 as part of the Rubin Early Science Program (Guy et al. 2026), established to provide the community with early access to data products and services needed to produce high-impact science during the period spanning commissioning through the first Data Release. Data Preview 0 (DP0) was based on simulated LSST-like data (LSST Dark Energy Science Collaboration (LSST DESC) et al. 2021) and served primarily to stand up early versions of the Rubin Science Platform (RSP) and prepare the community for data access at scale. Data Preview 1 (DP1) (NSF-DOE Vera C. Rubin Observatory 2025) delivered the first data products derived from on-sky observations using science-grade exposures acquired with Rubin Commissioning Camera (LSSTComCam) (Stalder et al. 2022, 2020; Howard et al. 2018; SLAC National Accelerator Laboratory & NSF-DOE Vera C. Rubin Observatory 2024); a 144-megapixel, single-raft instrument used during early commissioning prior to the installation of LSSTCam on the Simonyi Survey Telescope. DP2 supersedes both in scope, fidelity, and scientific depth.

DP2 contains X science-grade exposures acquired over 158 nights between 2025-04-16 and 2025-09-21, covering a total sky area of $\sim$15 deg$^2$ across X fields. The data products include raw and calibrated single-epoch images, coadded images, difference images, source detection catalogs, and a range of derived data products. The release totals approximately 59.15 TB and contains around X distinct astronomical objects. Full release documentation is available at https://dp2.lsst.io.

Because DP2 is drawn from a commissioning and early-operations data rather than from the more uniform and systematic LSST, its images and derived products reflect a system that was still being commissioned and tuned. LSSTCam's greater scale and complexity relative to LSSTComCam introduced systematics with no direct counterpart in DP1. For much of the campaign the Active Optics System (AOS) closed loop converged on a slightly mis-calibrated focus target, imprinting a spatially varying defocus across the focal plane that was only corrected on sky in December 2025 and that remains visible in the point-spread function (PSF) of a large fraction of DP2 exposures. Delivered image quality and PSF ellipticity did not consistently meet LSST design requirements in wide-area survey-mode observations by the close of commissioning; and stray- and scattered-light artifacts, sky-background systematics in crowded fields, and a chromatic PSF dependence[2] were identified and only partially mitigated in DP2 processing. These effects, their diagnosis, and the mitigations applied are described in §2 and §6.

Unlike the systematic, rolling revisit pattern that will characterize the LSST, DP2's observing cadence is opportunistic: fields and filters were prioritized to serve AOS and Science Pipelines commissioning rather than to build a representative time series. The Science Validation survey footprint was repeatedly re-scoped over the course of the science validation campaign due to the competing demands of engineering tests and filter availability, which was constrained by hardware issues for part of the campaign. Visit counts and time sampling therefore vary substantially and idiosyncratically from field to field, and DP2 should not be read as a preview of LSST's eventual survey cadence, revisit statistics, or depth-accumulation pattern.

DP2 is being delivered in two phases across the Jul–Dec 2026 window. The first phase, Early DP2 (EDP2), comprises the deep coadd images and all associated catalogs, including new cell-based coadds and the first releases of the An object with measurements using the metadetection algorithm, or the catalog thereof. (ShearObject) (§4.3.4) shape-measurement catalog and the Isolated Star Stellar Motions catalog. EDP2 is targeted for 2026-07-27. The second phase, DP2, adds the visit-level single-epoch and difference images, completing the full release, and is expected in the Oct–Dec 2026 range. Data products delivered as EDP2 will be incorporated into DP2 unchanged, without additional reprocessing (Guy et al. 2026). This phased delivery follows directly from Rubin's hybrid cloud architecture (O'Mullane et al. 2024), in which science data products are stored at the United States Data Facility (USDF)

[2] LSSTCam has no atmospheric dispersion corrector

and served to users via the US Data Access Center (DAC) in Google Cloud. Deep coadd images and catalogs are hosted directly in Google Cloud and are therefore unaffected by hybrid-cloud readiness, allowing them to ship as EDP2. Visit-level images, however, must be streamed from the USDF, and the necessary capacity is not yet fully in place, introducing timing uncertainty for the second phase. Delivery of the Prompt Data Products follows the same logic. The Prompt Products DataBase (PPDB), Rubin's real-time catalog of transient, variable, and moving-object detections, does not depend on USDF–Google Cloud bandwidth and is therefore prioritized as the second Early-Operations delivery milestone, following EDP2 and preceding the full DP2 release, expected in the Sep–Oct 2026 range. Prompt images (raw images, Processed Visit Images, and difference images), which do require that bandwidth, have been deprioritized relative to EDP2 and the PPDB and are expected to become available only in the Oct–Dec 2026 range, following both.

DP2, like all Rubin Data Previews and Data Releases, is subject to a 2 yr proprietary period; during this time access is restricted to LSST data rights holders (Blum & the Rubin Operations Team 2020) via the RSP (Jurić et al. 2019), Rubin's cloud-based data science platform (Jurić et al. 2019). After the proprietary period, DP2 will be made public, though access through Rubin DACs in the US and Chile will remain limited to data rights holders (Blum & the Rubin Operations Team 2020). Alternative public access mechanisms have not yet been finalized.

The structure of this paper is as follows. Section 2 describes the observatory system and its status at the close of commissioning, the fields included in DP2, and the observing strategy employed. Section 3 summarizes the data products in the release. The processing pipelines are described in Section 4, followed by data validation and performance characterization in Section 6. Section 7 describes the RSP. Section 8 outlines Rubin's community support model. A summary and outlook toward the start of formal LSST Data Releases is given in Section 9.

All magnitudes are quoted in the AB system (Oke & Gunn 1983) unless otherwise specified.

## 2. COMMISSIONING WITH LSSTCAM

## 3. OVERVIEW OF THE CONTENTS OF RUBIN DP2

## 4. DATA RELEASE PROCESSING

Data Release Processing (DRP) is the data pipeline that produces the calibrated images, detection catalogs, and derived data products defined in section §TBD, using the LSST Science Pipelines (citation). DP2 was processed at the United States Data Facility (USDF) at SLAC, with pilot runs at the National Institute of Nuclear and Particle Physics (IN2P3) computing center.

The processing campaign consists of four major stages: (1) single-frame processing, (2) calibration, (3) multi-visit processing, (4) variable and transient source processing. Data quality and key metrics for verification and validation are actively monitored during each stage, and comprehensive verification and validation assessments are completed before processing the next stage.

This section describes the high-level algorithms, configurations, and verification metrics for each stage, including changes and improvements from DP1 (citation).

### 4.1. *Single-Visit Processing*

#### 4.1.1. *Calibration & Instrument Signature Removal (ISR)*

The first task in data processing begins with a raw image. This image is in integerized analog-to-digital units (ADU, or counts) and contains detector artifacts imprinted by the physics of the detector and readout hardware. This step aims to remove any artifacts that are not of astrophysical origin and produce science-ready, single-visit exposures in floating-point electron units with complete pixel masks.

The ISR pipeline is built on a physical model of the detectors and readout electronics, in which each artifact is tied to a specific point in the photon-transfer chain and is corrected using calibrations from dedicated campaigns conducted during the day or on cloudy nights. Figure 1 shows this model of the detector and readout components and the effects each imparts on the measured image. ISR works backward through the chain, undoing these effects in the reverse of the order in which they were imprinted.

Detector response and performance vary across the focal plane, and more so for LSSTCam than for ComCam during DP1 processing. The full LSSTCam focal plane comprises 189 science charge-coupled devices (CCDs) from two vendors (Imaging Technology Laboratories, ITL, and Teledyne e2v, E2V), each of which must be processed separately.

A detailed description of the DP2 ISR procedures and the calibration products they consume can be found in (Cite RTN-117 here when DOI becomes available).

The ISR processing pipeline for DP2 performs the following steps, in order: (1) conversion of the raw integers to floating point, (2) ADU dithering to mitigate quantization effects, (3) serial overscan subtraction, (4) saturated- and suspect-pixel masking, (5) gain (electrons/ADU) correction, (6) crosstalk correction, (7) parallel overscan subtraction, (8) non-linearity correction, (9) deferred-charge correction, (10) vendor-specific

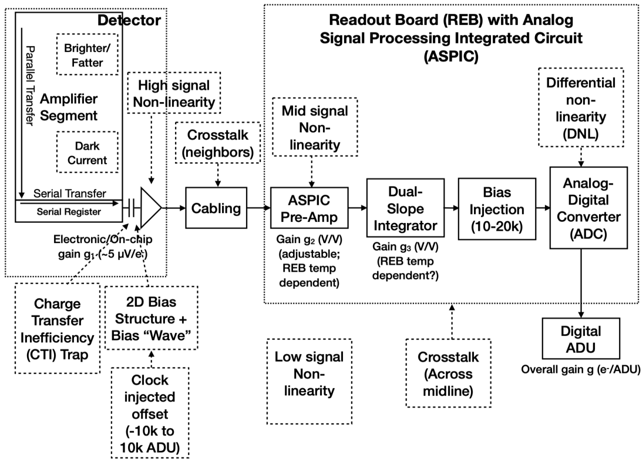


**Figure 1.** The model of the detector and REB components, labeled with the effects that they impart on signal.

masking (E2V edge bleed; the ITL "dip," saturation sag, and edge bleed), (11) bias subtraction, (12) dark subtraction, (13) defect masking, (14) saturated pixel footprint widening, (15) brighter-fatter correction, (16) variance plane estimation, (17) flat fielding, (18) interpolation over masked pixels, (19) amplifier-offset corrections.

Each calibration must be valid for the conditions under which the science image was taken. Camera power cycles, large temperature shifts, and changes to the CCD operating mode (sequencer) can all invalidate earlier calibrations. Over the DP2 observing period, calibration products are therefore organized into three calibration epochs. Epoch 1 (April 24–July 2, 2025) covers the initial on-sky commissioning period with the `2s_v30` sequencer, using defect maps derived from in-lab calibration campaigns conducted before the camera was installed on the telescope. Epoch 2 (July 3–September 21, 2025) used an updated `3s_v1` sequencer, which lowered the saturation point but reduced read noise, crosstalk, and charge persistence relative to Epoch 1. Following an observatory maintenance shutdown in October, Epoch 3 (October 24, 2025–January 6, 2026) resumed under the same sequencer but used a new set of calibrations. A fourth epoch, not included in DP2, began January 23, 2026 with the `3s_v2` sequencer, bringing reduced correlated noise and improved linear readout response.

Compared to DP1 (Vera C. Rubin Observatory Team 2026), the ISR pipeline has been substantially upgraded, including improved sensor diagnostics and characterization, an entirely new brighter-fatter correction based on Astier & Regnault (2023) and Broughton et al. (2024), and an all-new flat-field production pipeline that corrects for gradients and mis-centering of the flat-field illumination using new calibration hardware. A new set of 10 LEDs spanning the full sensitivity range of the LSSTCam sensors (one in $u$, two each in $griz$, and a new 1050 nm LED shared between $y$ and $z$). For the bands covered by two LEDs, we combine separate flats for each LED (for the blue and red side of the band) into a so-called "anaglyph" flat, with a weighting that approximates a flat spectral energy distribution across the band.

ogether, these upgrades allow ISR to deliver uniform, science-ready exposures across all 189 LSSTCam science sensors for DP2.

#### 4.1.2. *Background Subtraction*

Background subtraction in `CalibrateImageTask` estimates and removes large-scale background signals from science imaging prior to source detection and measurement. Such signals include sky brightness from airglow, moonlight, scattered light, zodiacal light, and diffuse astrophysical emission. The background is estimated twice: an initial model (`psf_subtract_background`) is subtracted before PSF characterization, and a second model (`star_background`) is fit on the updated source-masked image before the final detection pass. Each post-ISR image is divided into $128 \times 128$ pixel superpixels, and the iterative $3\sigma$-clipped mean of unmasked pixels in each bin is fit with a sixth-order two-dimensional Chebyshev polynomial, evaluated at native pixel resolution via Akima spline interpolation. Before fitting `star_background`, the `DETECTED` mask plane is dilated by up to 10 pixels to suppress source-wing flux from leaking into background bins. After `star_background` subtraction, a zeroth-order pedestal correction is estimated iteratively over bin sizes starting at $32 \times 32$ pixels, doubling each step until the cumulative pedestal level changes by less than 5% or 0.5 counts between steps. The `star_background` model and pedestal corrections together constitute the output background model (`preliminary_visit_image_background`; see Figure 2).

Compared to DP1 (NSF-DOE Vera C. Rubin Observatory 2025), several changes were made to background subtraction for DP2. The inline re-estimation performed after each detection pass in DP1 (`reEstimateBackground = True`) has been replaced by the dedicated `star_background` subtask. In addition to source mask dilation and a pedestal correction, other new features for DP2 include adaptive threshold determination and diffraction spike masking. The per-step illumination correction used in DP1 has been disabled for DP2. Following background subtraction, the median and standard deviation of all unmasked pixels and

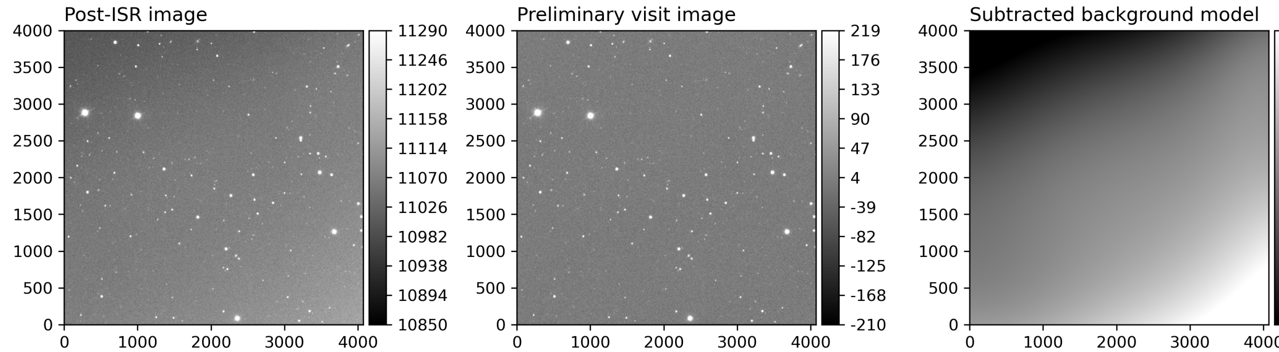


**Figure 2.** Background subtraction for LSSTCam visit 2025110500300, detector 25. *Left:* Post-ISR image (`post_isr_image`), before any background removal. *Center:* Preliminary visit image (`preliminary_visit_image`), after background subtraction by `CalibrateImageTask`. *Right:* The subtracted background model (`preliminary_visit_image_background`), illustrating the large-scale structure removed. All three panels use a linear stretch clipped to the central 95th percentile of pixel values.

of *sky source* fluxes are recorded in the task metadata as diagnostics of background subtraction quality.

## 4.2. *Calibration*

### 4.2.1. *PSF Modeling*

PSF modeling in DP2 uses two distinct approaches, as described in the (Rubin Observatory Science Pipelines Developers 2025) and it is similar to what was originally described in DP1 The first model—faster but less precise—is fit with PSFEx (Bertin 2011), while the final model—slower yet more accurate—is fit with Piff (Jarvis et al. 2021). Broadly speaking, PSFEx and Piff both represent the PSF on a pixel basis and interpolate its parameters across a single CCD using two-dimensional polynomials. However, their technical implementations differ (see Bertin et al. and Jarvis et al. 2021 for more details). Previous comparisons have shown that Piff outperforms PSFEx by delivering an unbiased reconstruction of the PSF size (see Zuntz et al. 2018 and Jarvis et al. 2021), can work in sky coordinates like in Schutt et al. 2025, can include a color dependency like in Schutt et al. 2025, and is supporting alternative models and interpolation schemes (see Schutt et al. 2025 for more details).

In the initial PSF modeling pass, PSFEx is run with a pixel basis and a second-order polynomial interpolation on each CCD. For the final modeling, Piff uses its PixelGrid with a fourth-order polynomial interpolation per CCD—except in the u-band, where star counts are too low to constrain a fourth-order fit, so a second-order polynomial is used instead. Both are working in pixel coordinates. Choices of polynomial order, overall PSF-modeling performance, and known issues are discussed in Section "Performance and Known Issues for PSF."

### 4.2.2. *Astrometric Calibration*

The final astrometric calibration of the data follows the method in DP1, but with some key additions. As described in DP1, a joint calibration is performed on all visits in a given band overlapping a given area. By associating all the isolated point sources shared among the overlapping visits, we can refine the astrometric solution beyond the level achieved in single-frame processing using only a reference catalog.

Unlike in DP1, the area we use for individual fits of the astrometric solution is an order-3 healpix, instead of a tract. This is done to reduce repetitive calculations, since the small size of tracts compared to the LSSTCam field of view means that neighboring tracts often share identical overlapping visits, which would lead to doing many identical fits of the astrometric calibration.

As in DP1, the astrometric model consists of a static map from pixel space to an intermediate frame, which is followed by a per-visit map from the intermediate frame to the plane tangent to the telescope boresight, and finally a deterministic mapping from the tangent plane to the sky. This is done by the `gbdes` package (Bernstein et al. 2017), as described in Saunders (2024). The proper motion and parallax of the objects used in the calibration are fit as part of the solution, but we do not yet include differential chromatic refraction or lateral color. These will be included in future data releases during Rubin Operations.

The main difference from the DP1 astrometric calibration is an additional step that models the effect of atmospheric turbulence on the astrometry. The per-visit part of the astrometric model already described captures large-scale variation between visits, which includes some atmospheric effects. However, higher order oscillations are visible in the astrometric residuals, and these can be attributed to atmospheric turbulence (Saunders 2025).

As described in Fortino et al. (2021) and Léget et al. (2021), the wave-like astrometric effects caused by turbulence can be modeled by a Gaussian process. In DP2, we do this by taking the astrometric residuals remaining after the `gbdes` fit, grouping them by visit, then modeling them with the Gaussian Process package `treegp`. We then use this Gaussian Processes model to predict the effects of turbulence on a grid. Finally, this grid is turned into a two-dimensional spline that can use the AST component `SplineMap` so that it can be concatenated with the `gbdes` model. By including this model for the higher-order atmospheric turbulence, we achieve a significant improvement in the astrometric calculation, as demonstrated in Section 6.

A corollary product of the `gbdes` astrometric calibration is the catalog of proper motions and parallaxes of the sources used in the calibration. Since the `gbdes` fit is done per-band, and then improved by the turbulence fit, we perform an additional final fit of the proper motion and parallax, using the final astrometric model and all available bands. The resulting catalogs are included in the DP2 data release. These catalogs only include isolated point sources, but future data releases will be extended to include proper motion and parallax for all objects.

#### 4.2.3. *Photometric Calibration*

Photometric calibration of the DP2 dataset is based on the Forward Global Calibration Method (FGCM Burke et al. 2018) adapted for the LSST Science Pipelines (Aihara et al. 2022; Fagrelius & Rykoff 2025). We used the FGCM to calibrate the full DP2 dataset with a forward model that uses a parameterized model of the atmosphere as a function of airmass along with a model of the instrument throughput as a function of wavelength. The FGCM process typically begins with measurements of the instrumental throughput, including the mirrors, filters, and detectors. For the LSSTCam filter throughputs, we start with the filter scans provided by the manufacturer, Matereon. These were taken in a grid with 159 positions, at 5 incidence angles from 13.8 to 23 degrees, at a wavelength resolution of 1 nm. We performed an averaging procedure to get the approximate appropriate throughput for the LSSTCam beam as it intersects the filter at the central location of each detector. For the LSSTCam detector quantum efficiency (QE) curves, we start with per-raft measurements of the QE performed at Brookhaven National Laboratory (BNL) and SLAC National Accelerator Laboratory (SLAC) at 10 to 25 wavelength steps. These preliminary scans were then normalized relative to each other at 750 nm. However, there are still some per-raft systematic differences seen, particularly in the u and y bands. In the future we will use the in-dome tunable laser system and the Collimated Beam Projector (CBP) for improved filter and detector throughputs.

The FGCM atmosphere model, provided by MODTRAN (Berk et al. 1999), was used to generate a look-up table for atmospheric throughput as a function of zenith distance at Cerro Pachón. This model accounts for absorption and scattering by molecular constituents of the atmosphere, including O2 and O3; absorption by water vapor; and Mie scattering by airborne aerosol particulates. Nightly variations in the atmosphere are modeled by minimizing the variance in repeated observations of stars with an SNR greater than 10, measured using "compensated aperture fluxes." These fluxes include a local background subtraction to mitigate the impact of background offsets. The model fitting process incorporates all six bands (*ugrizy*) but does not include any gray (achromatic) terms, except for a linear assumption of mirror reflectance degradation and dust accumulation on lenses. Fortunately, there is no evidence of any signficant loss of throughput over the 250 days of the DP2 dataset. As an additional constraint on the fit, we use a subset of stars from the Monster reference catalog (Ferguson et al. 2025), primarily to constrain the system's overall throughput and establish the "absolute" calibration.

### 4.3. *Multi-Visit Processing*

#### 4.3.1. *Input Data Selection*

Detectors 0, 20, 27, 65, 123, 161, 168, 188 are excluded from the `deep_coadd` images. Only exposures with a seeing better than 1".8 FWHM are included in the `deep_coadd` images. Exposures with poor PSF modeling, identified using internal diagnostics, are also excluded from the `deep_coadd` images to prevent contamination of the coadds with unreliable PSF estimates.

#### 4.3.2. *Coaddition*

The single visit images that pass the selection criteria above are warped onto the coadd pixel grid using Lanczos3 kernel and scaled to have units of `nJy` (zeropoint of 31.4). Artifacts are identified and masked in a manner similar to DP1 before coaddition. We apply the artifact rejection procedure described in AlSayyad (2018), which identifies and masks features such as satellite trails, optical ghosts, and cosmic rays. It operates on a time series of PSF-matched images resampled onto a coadd pixel grid ("warps") and leverages their temporal behavior to distinguish persistent astrophysical sources from transient artifacts. Artifact rejection uses both direct (where no PSF matching is performed) and PSF-matched warps, homogenized to a standard PSF of 1.8

FWHM, broadly consistent with the 1.7 FWHM seeing threshold used in data screening. A sigma-clipped mean of the PSF-matched warps serves as a static sky model, against which individual warps are differenced to identify significant positive and negative residuals. Candidate artifact regions are classified as transient if they appear in fewer than a small percentage of the total number of exposures, with the threshold based on the number of visits These masks are also saved as the `compare_warp_artifact_mask` dataset.

In DP2, the coadded images are cell-based, using the `lsst_cells_v2` skymap. Coadds are built as weighted averages of the input warps. Each detector is assigned a weight that is the inverse of the mean of the variance reported in the `visit_summary` dataset. Following Armstrong et al. (2024) for each cell in the coadd, a detector is excluded if its geometry does not overlap the cell completely. Furthermore, a detector is excluded if more than 50% of its pixels are masked as artifacts, unless it would result in an empty cell in which case, this condition is ignored. Finally, pixels that did not get any contribution from the input visits are interpolated from neighboring pixels.

A key difference between cell-based coadds and coadds in DP1 is in the PSF representation. Single visit PSFs are evaluated at point corresponding to the center of cells and warped into a 35x35 postage stamp, which ensures that at least 99.5% of the flux is captured. These postage stamps are then weighted by the same weights used for the coadd and averaged. The PSF within the cell is approximated as spatially constant. The pixels that have artifacts from any of the input visits have `INEXACT_PSF` flag set to denote that the PSF of those pixels may differ from that attached to the cell. The metadata about which visits contribute to the cell, what fraction of pixels are unmasked, PSF summary statistics are stored.

#### 4.3.3. *Detection, Deblending, & Measurement*

Coadd detection and measurement proceeds with a similar order of steps as in DP1; however, numerous changes have been made to individual algorithms. The main change is that algorithms run on cell-based coadds, which have fewer PSF discontinuities within cells. For this release, though, none of the measurement algorithms take cell boundaries into account, and those that require a PSF model use the PSF model at the centroid of the object (and therefore of the cell that the centroid is within) for all cells.

First, peaks are detected in single-band patch images. These peaks are then merged across bands to produce a multiband peak catalog. This catalog is used as an input for deblending, which outputs deblended (but not deconvolved) images for each object. All object catalog measurements are performed on these deblended images.

The basic methodology for detection is largely unchanged from the description in Bosch et al. (2018), which we summarize here. To detect peaks, each image is convolved by a circular Gaussian approximation to the measured PSF to make a significance image. A footprint is a contiguous region of pixels above the detection threshold, which is set to detect isolated point sources above $5\sigma$ significance. Footprints can have multiple peaks, which are defined as pixels with values higher than all 8 neighbours (local maxima within a 3x3 box). Note that even for an isolated object, the significance of a detection is not precisely the same as the signal-to-noise from subsequent PSF model fluxes.

Pixels within footprints are marked with the DETECTED bit mask. The remaining pixels are used for background estimation and subtraction, excluding significantly negative-valued pixels which are likely to be residual artifacts. The algorithm also attempts to randomly place 100 "sky objects" within the noise-dominated pixels, reducing the number in crowded fields with low numbers of sky-dominated pixels if necessary. These objects do not appear in the final object catalog but are used to characterize the sky variance in intermediate steps.

As explained in Aihara et al. (2019), the process of convolving the image by an approximation of the PSF reduces the variance in the image, and therefore the pixel significance threshold must be adjusted to achieve the desired detection threshold. This factor is computed by measuring the standard deviation of the PSF model Signal to Noise Ratio (SNR) of the sky objects.

Once detection has run in each available band, footprints and their peaks are merged in a fixed priority order, *irzygu*, which is roughly in order of expected SNR for typical objects. New peaks are only added if they are at least $1\farcs0$ further than an existing peak, and existing peaks are marked as detected in multiple bands if a new peak is found within $0\farcs3$; peaks within this range are ignored. After merging, probable spurious peaks detected in only one band are removed.

Deblending is performed by the The "lite" version of the scarlet algorithm, optimized for multiband deblending on pixel-aligned grids. Includes the scarlet_lite and meas_extensions_scarlet Python packages. (scarlet lite) python package. scarlet lite is an optimized implementation of the scarlet (Melchior et al. 2018) deblending algorithm with the assumption that the input images are aligned to the same pixel grid at a fixed resolution, as is the case in coadds. Prior to deblending, a new addition in DP2 is a per-band partial deconvolution of the input coadds to a common $\sigma = 0.8 pixel$ integrated circular Gaussian PSF. This allows us to sub-divide large parent blends (footprints) into multiple smaller blends that are only connected by the wings of the PSF. These smaller sub-blends and the initialization of galaxy morphologies from the partially deconvolved images improves numerical convergence and performance, both in the goodness-of-fit of the final models and in memory usage and runtime. Users will notice that this has improved our coverage in crowded fields from DP1; however, in the densest fields, an entire patch can still be a single blend and must be skipped due to excessive memory requirements.

Object measurements are conducted in three modes: independent per-band measurements, forced measurements in each band, and multiband measurements. As detailed in Bosch et al. (2018), measurement first replaces all pixels in footprints with noise, so that algorithms that require pixel values beyond footprint boundaries can perform measurements without contamination from neighbors (whether they are part of the same blend or not). During measurement, isolated objects have their original pixel values inserted back into the image, while blended objects use the scarlet lite models as templates to re-distribute the original image values. This preserves the flux from the original image where objects have no overlap and dampens the noise elsewhere, since the flux is reapportioned to multiple objects.

The single-band measurement plugin system remains unchanged from DP1 and largely follows the description in Bosch et al. (2018). Measurements are made in every available band, and a reference band is defined from the same priority order as detection merging (*irzygu*) for a second round of forced measurements. These use the shape and position from the reference for consistency. Most algorithms have their free measurements reported in the final object table, but forced values are generally recommended.

A variety of flux measurements are provided, including aperture fluxes, Kron (1980), and Gaussian-Aperture-and-PSF (Gaussian Aperture and PSF (GAaP) Kuijken 2008; Kannawadi 2025) fluxes for consistent galaxy colors. Forward Point Spread Function (PSF) model and Composite model (CModel) magnitudes (Abazajian et al. 2004; Bosch et al. 2018) are provided for each band.

The MultiProFit astronomical source modelling code, including the multiprofit Python package and its dependencies, and the meas_extensions_multiprofit package for pipeline tasks. (MultiProFit) (Taranu 2025) performs multiband forward modelling. Beginning in DP2, an exponential profile is fit first and used to initialize a subsequent Sérsic model (Sérsic 1963; Sersic 1968) fit, which improves convergence and reduces the prevalence of Sérsic fits with unrealistically large effective radii. Both exponential and Sérsic model fits have free centroids, which serve as alternative, multiband astrometry for objects. The Object table now includes uncertainties on the fitted ellipse parameters for both models (the x- and y-axis effective radii and correlation parameter $\rho$). These will be converted to uncertainties on more commonly used parameters (major/minor effective radii and axis ratios) for DR1.

Some additional derived parameters are included in the object catalog, mainly for object classification. "extendedness" is a binary classifier, set to 1 if the PSF to CModel flux ratio is below 0.985. "sizeExtendedness" is a quasi-probabilistic morphological classifier reported as $1 - exp(-0.5 * ((T_{HSM} - T_{PSF})/T_{PSF}^{0.5})^2)$, where $T_{HSM}$ and $T_{PSF}$ are the sum of the squares of the x- and y-axis moments for the object from the HSM algorithm and for the PSF model, respectively. As an alternative, DP2 adds model_extendedness, which is a continuous, heuristic classifier that uses both the exponential model effective radius and the ratio of the Sérsic model to PSF model flux. It is available for each band and separately for the sum of the *griz*-band fluxes.

As for DP1, photometric redshifts are not computed or included in the object table but are planned as a supplementary user-generated product.

Further details on the performance of these algorithms are found in TODO: add relevant section references.

#### 4.3.4. *Metadetection and ShearObject*

The ShearObject catalog using the multiband metadetection algorithm (Sheldon et al. 2020) is new to DP2. It creates an entirely separate catalog with detections that do not correspond to the Object catalog. Each 150x150 cell in 'griz' bands is extracted with a 50 pixel border to make 250x250 pixel images, that are then passed to metadetect. Internally, metadetect makes counterfactual images by deconvolving by the original PSF, shearing the image and reconvolving to a new PSF using the `fitgauss` reconvolution algorithm. Metadetect coadds 'riz' bands to form a coadd for detection, and measures shear using the `gauss` algorithm by fitting a 2D elliptical Gaussian to $r$, $i$, $z$ coadds. Additionally, for these detections, it also reports force-photometered fluxes in $g$, $r$, $i$ and $z$ bands for these detections measured using the `pgauss` algorithm. There is no deblending performed prior to these measurements.

#### 4.3.5. *First Look*

### 4.4. *Variable & Transient Source Processing*

#### 4.4.1. *Difference Image Analysis (DIA)*

DP2 difference imaging analysis did not change significantly relative to DP1. DP2 Difference Image Analysis (DIA) uses the decorrelated Alard and Lupton image differencing algorithm (Alard & Lupton 1998; Reiss & Lupton 2016). Both positive and negative `DIASource`s are detected in the difference image at $5\sigma$. We fit a dipole model to sources containing both positive and negative peaks, and infer trail parameters from the second moments of the PSF. After rejecting likely artifacts (§4.4.2), we associate `DIASource`s into `DIAObject`s with a $1''$ matching radius.

#### 4.4.2. *Artifact Rejection*

DIA analysis is prone to false positives. We employ several layers of artifact rejection, although we err on the side of completeness rather than purity in Data Release Processing.

As in DP1, prior to writing the `DIASource` catalog, we remove sources with pixel flags artifacts, non-astrophysical trail lengths, and unphysically negative direct fluxes. In DP2 we also reject sources that land on the modeled positions of diffraction spikes and apply morphological cosmic ray rejection on both the direct and difference images. Further, we flag but do not remove multiple `DIASources` that occur in a straight line with `glint_trail`, indicating that they may be due to rotating orbital debris (Karpov & Peloton 2022).

We developed a machine-learned reliability score to assess whether `DIASources` were astrophysical. (Acero-Cuellar et al. 2026) provides an overview of the model architecture, training, and performance of the real-bogus model. The v0.1 model used in DP1 was again used during DP2 processing. No cuts were applied on reliability for the DP2 `DIASource` catalogs, so users interested in higher purity should apply a minimum reliability threshold.

#### 4.4.3. *Light Curves*

As with DP1, multi-epoch forced photometry is performed on both the visit images and the difference images. For users interested in light curve construction, we recommend using the forced photometry performed on the difference-images (the psfDiffFlux column of the ForcedSource table), since this measurement isolates the time-variable component of the flux and is unaffected by contamination from non-varying nearby sources. Forced photometry carried out directly on the visit images, by contrast, may pick up flux from blended or nearby static objects, and the severity of this contamination depends on the seeing. The centroids adopted for this multi-epoch forced photometry step are drawn either from coadd-based object positions or from the DIAObjects, which are constructed from the DIASources associated from detections in the difference images.

## 5. SOLAR SYSTEM DATA PRODUCTS

### 5.1. *Overview*

The DP2 solar system data products concentrate on associations between Rubin `DiaSource` observations and previously known objects. These are known-object products, not a blind moving-object search or an orbit catalog derived from DP2 alone. This release delivers observations whose positions were associated with objects in the Minor Planet Center (MPC) orbit catalog, as described in Section 5.2, together with a Rubin-derived catalog of object-level photometry, including per-band absolute magnitudes, in the `SSObject` table.

Rubin also searched for and discovered new solar system objects in Prompt Processing. That discovery campaign preceded the official DP2 Data Release processing so that newly reported objects entering the MPC catalog before the cutoff could be treated as known objects during association. Consequently, objects first discovered by Rubin can occur in these products, but DP2 does not deliver a standalone catalog of Rubin discoveries. The Prompt Processing discoveries will be described in a forthcoming series of papers, and future Data Releases will deliver catalogs of Rubin discoveries.

DP2 provides five solar system tables (Table 1). Two are derived from the Rubin observations: `SSSource`[3] contains one row per associated detection and links measured `DiaSource` photometry and astrometry to a predicted object, while `SSObject` contains one row per object and summarizes its observations, per-band photometric properties, and selected orbit-derived quantities. The Rubin-derived tables contain 8,149,633 `SSSource` rows for 299,819 distinct objects, with the same 299,819 objects represented in `SSObject`. Every `diaSourceId` occurs at most once.

The other three products are auxiliary snapshots of tables in the MPC PostgreSQL database. They provide reference catalogs for orbital information and object cross-identification, retaining the upstream MPC semantics rather than being recomputed from DP2 observations. Their field definitions are documented in the MPC schema for the PostgreSQL tables replicated

[3] Rubin will submit the astrometric measurements represented in `SSSource` to the MPC in stages, allowing the association quality to be validated before each submission and minimizing the risk of reporting misassociations.

**Table 1.** Delivered DP2 Solar System Tables

| Table | Rows | Columns | Intent and useful relations |
|---|---|---|---|
| `SSSource` | 8,149,633 | 39 | One row per associated `DiaSource`, containing measured and predicted single-epoch quantities. Join by `diaSourceId` to the detection and by `ssObjectId` or `designation` to object-level tables. |
| `SSObject` | 299,819 | 80 | One row per recovered known object, including sampling summaries, phase-curve fits, and selected quantities derived from the input orbit. |
| `mpc_orbits` | TBD[a] | 53 | MPC snapshot of orbital elements, fit metadata, uncertainties, and MPC photometric parameters. The convenience `designation` column supports direct joins to the Rubin-derived tables. |
| `current_identifications` | TBD[a] | 11 | MPC mapping between primary and secondary provisional designations that refer to the same physical object; useful for resolving aliases. |
| `numbered_identifications` | TBD[a] | 11 | MPC mapping between permanent numbers and primary provisional designations, with IAU designations, names, credits, and publication references where available. |

[a] Insert the row count from the final DP2 MPC snapshot. The source tables were not available to this drafting repository, and current live-MPC counts would not describe the delivered snapshot.

through the Small Bodies Node.[4] The `mpc_orbits` table records the MPC orbit solution and associated fit information for designated objects. The `current_identifications` table identifies primary and secondary provisional designations that refer to the same object, and `numbered_identifications` connects an object's permanent number to its primary provisional designation. The former includes both self-mappings ($A = A$) and links among aliases ($A = B$); the latter also carries IAU naming information when available. The `mpc_orbits` table available at ingestion did not contain comets. Because the predictions used for association were generated from that snapshot, no comets were available to be associated with DP2 detections and none occur in the delivered `SSSource` or `SSObject` products.

In `SSSource`, `SSObject`, and `mpc_orbits`, `designation` denotes the unpacked primary provisional designation of the object. This column was added to the delivered `mpc_orbits` copy as an end-user convenience; there it is identical, row by row, to `unpacked_primary_provisional_designation`. It therefore provides a readable and direct join key among `SSSource`, `SSObject`, and `mpc_orbits`, without requiring users to unpack MPC designations. For query performance, users should nevertheless prefer SQL joins on integer identifiers such as `ssObjectId` wherever those identifiers are available, and use `designation` for readability or when an appropriate integer key is unavailable.

[4] https://docs.minorplanetcenter.net/mpc-ops-docs/data-and-services/replicated-tables-schema/

### 5.2. *Association and the `SSSource` Product*

The association input was a 2025 March 13 snapshot of the MPC orbit database[5], limited to objects whose observational arcs exceeded two days. Associations were made independently for each detector and visit using positions predicted by Sorcha (Merritt et al. 2025; Holman et al. 2025) at the visit epoch from this orbit catalog. Predicted objects were first restricted to the detector footprint. Measured `DiaSource` coordinates were represented as unit vectors on the celestial sphere and stored in a $k$-d tree. For each predicted position, the algorithm identified the nearest detection within $1''$. Candidate pairs were considered in increasing separation, accepting a pair only if neither member had already been assigned. Thus, this is a positional, one-to-one match; it uses neither brightness, color, morphology, nor rate and does not calculate a probabilistic association score. The delivered `diaDistanceRank` is set to one for every row and should not be used as a measure of match ambiguity. Chance associations remain possible because the match does not use brightness or detection reliability, and are more likely where the `DiaSource` density is high. Users constructing a high-purity sample should consider detection reliability, angular and cross-track residuals, consistency with the predicted magnitude, and the uncertainty of the input orbit. Detection-level reliability information requires the join to `DiaSource` described below.

Each accepted row carries the measured position and the Sorcha ephemeris position, the measured PSF pho-

[5] Small bodies discovered after 2025 March 13—including those found in Rubin data—are therefore absent from the `SSSource` table delivered here.

tometry and band, the predicted apparent $V$-band magnitude, phase angle and solar elongation, heliocentric and topocentric distances, sky-plane and radial rates, and Cartesian position and velocity components. R.A. and decl. are in degrees in the ICRS frame; the observation epoch `DIA_midpointMjdTai` is an MJD on the TAI time scale. Distances are reported in au, velocities in $\mathrm{km\,s^{-1}}$, sky rates in $\mathrm{deg\,day^{-1}}$, and residuals in arcseconds. State vectors are equatorial and evaluated at the light-emission (retarded) time. External comparisons must convert DP2 TAI epochs to the service's time scale; at a representative main-belt rate, neglecting the 37 s TAI–UTC offset produces a $\sim 0.23''$ shift.

`SSSource` is an association and ephemeris product rather than a copy of the complete `DiaSource` record. Although it contains selected measured quantities, users requiring the full detection-level measurements and quality information should join to `DiaSource` using `diaSourceId`. Each `diaSourceId` occurs at most once in `SSSource`, while unassociated `DiaSource` detections have no corresponding `SSSource` row. The ephemeris coordinates and state vectors in `SSSource` describe the predicted object at the observation epoch and should not be interpreted as a Rubin-derived orbital solution.

The matched-position residuals are strongly concentrated inside the adopted radius (Figure 3). The median radial offset is $0.071''$, while the median coordinate offsets are $-9.2$ mas in R.A. and $-22.7$ mas in decl.. Only 30 of the 8.15 million associations have offsets at or above $0.9999''$. The along-track and cross-track distributions are narrowly centered near zero, with medians of approximately 10 and 11 mas, respectively. As an external check, one representative epoch for each of 1000 well-determined, numbered asteroids was compared with JPL Horizons. Median separations were approximately 27 mas for the DP2 prediction relative to JPL, 26 mas for Rubin relative to JPL, and 39 mas for Rubin relative to the DP2 prediction.

A broader analysis of approximately 700,000 Rubin measurements of 65,000 known objects finds two regimes. For long-observed objects discovered before 2000, the median measured-minus-predicted coordinate residuals are below 1 mas, with a scatter of approximately 13–14 mas, comparable to the astrometric repeatability for bright stars. Objects discovered during 2000–2020 show a different pattern: offsets relative to JPL Horizons are spatially coherent across the DP2 footprint. In $5^\circ \times 5^\circ$ sky cells, the median offset-vector length is approximately 19 mas, the 95th percentile is approximately 30 mas, and the largest values approach 42 mas. Our current hypothesis is that orbit catalogs can carry 20–40 mas systematic errors in predicted positions, particularly in the southern hemisphere, because many orbits were constrained primarily by northern, pre-Gaia astrometry. The effect appears to diminish for objects discovered in the Gaia era. This interpretation remains under investigation and will be discussed in detail in a subsequent paper.

The observations span a wide range of sampling and geometry. There are 17,528 objects with a single associated detection, 31,873 with at most two, 212,181 with at least ten, and 7,293 with at least 100. The main belt dominates the distance and rate distributions, but the table includes 35 objects observed beyond 50 au, 765 source records at topocentric distances below 0.1 au, and 2,105 records with predicted rates above $1\,\mathrm{deg\,day^{-1}}$. Its ecliptic-latitude range, $-69.4^\circ$ to $+13.3^\circ$, primarily reflects the southern DP2 footprint rather than the intrinsic solar system distribution.

The `ephVmag` field is an approximate predicted Johnson $V$ magnitude derived from the input catalog photometric parameters. It is not a prediction in the Rubin band of the associated detection, so comparisons to the measured *ugrizy* photometry include both object color and phase-model differences (Figure 4). One delivered record for 2015 GE86 has `ephVmag`= 104.6 because the input absolute magnitude was the MPC missing-value sentinel $H = 99.99$; this value should be treated as missing rather than physical.

### 5.3. *Object-level Photometry and Phase Curves*

The `SSObject` photometric fields were derived independently in each of the *ugrizy* bands from PSF fluxes in the associated detections. For a flux $f$ in nJy, the conversion used was $m_{\mathrm{AB}} = 31.4 - 2.5\log_{10} f$, with magnitude uncertainty $1.085736\,\sigma_f/f$. Non-positive fluxes therefore yield non-finite magnitudes and were removed before fitting. Apparent magnitudes were reduced to unit heliocentric and topocentric distance using $m(1, 1, \alpha) = m - 5\log_{10}(r\Delta)$, where $r$ and $\Delta$ are in au.

The reduced magnitudes were described with the $H, G_{12}$ phase function of Muinonen et al. (2010). The DP2 processing fixed $G_{12} = 0.5$ and fit only the absolute magnitude $H$, since the short observing interval and limited phase-angle coverage do not generally support a stable two-parameter fit. Accordingly, valid per-band `G12` values are all 0.5, while `G12Err` and the $H$–$G_{12}$ covariance are undefined. A 0.05 mag uncertainty floor was added in quadrature to the measurement uncertainties to reduce sensitivity to unmodeled scatter, including rotational variability. After removing non-finite magnitudes, an initial fit with a robust loss was used to reject residuals beyond $10\sigma$, followed by a conventional least-squares fit to the retained observations. The per-band

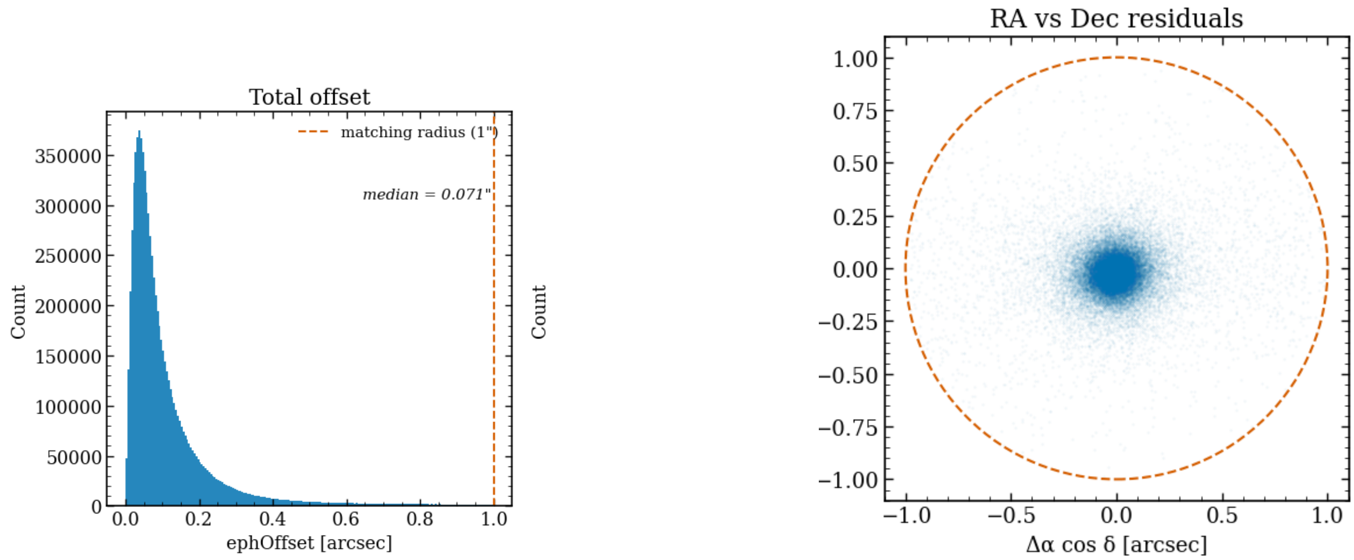


**Figure 3.** Astrometric properties of the associations. The distribution of accepted angular separations (left) and measured-minus-predicted R.A./decl. offsets for a reproducible random subset of 50,000 associations (right). The dashed circle marks the $1''$ association radius. The raster panels are taken from the validation notebooks and will be regenerated from the final parquet tables for publication.

`nObsUsed` field records the retained count and should be compared with `nObs` when assessing clipping or invalid photometry.

Valid $H$ estimates were obtained for 35,268, 196,015, 224,888, 231,890, 203,341, and 90,789 objects in *ugrizy*, respectively. Among objects with sufficient observations for a fit, failures range from 53 in $y$ to 1,034 in $g$, or less than approximately 0.5% in every band. Depending on band, 1–5% of the eligible measurements were removed as invalid or clipped. There are 25,706 objects with no fitted $H$ in any band; many are represented by only one detection and hence have insufficient information for a fit. The median fitted $H$ values are 18.7, 18.2, 17.5, 17.3, 17.2, and 16.6 mag in *ugrizy* (Figure 4). These distributions are dominated by main-belt objects and are also shaped by the DP2 footprint, cadence, phase-angle coverage, and band-dependent detection selection; they should not be interpreted as intrinsic population size distributions.

The quoted `HErr` values are covariance-derived under the fixed $G_{12}$ model and 0.05 mag error floor; they do not include uncertainty in phase-function shape or a physical model of rotation. Fits based on two or three detections are more model-dependent than fits spanning many epochs and a broad phase-angle range. Users should therefore select on `nObsUsed`, inspect `phaseAngleMin` and `phaseAngleMax`, and treat poor fits or discordant bands as possible signs of sparse sampling, variability, blending, or misassociation. A substantial high-value tail in the per-band $\chi^2$ per degree of freedom likewise shows that the adopted model and uncertainty floor do not capture all of the observed variability. Moreover, observations in different bands were generally not simultaneous, so colors formed from the fitted per-band $H$ values can include rotational variability and should not be interpreted as instantaneous colors.

The resulting cross-band colors are broadly plausible for an asteroid sample: the medians are approximately $g - r = 0.58$, $r - i = 0.18$, and $i - z = -0.01$ mag. The tails are driven by sparse fits: of 721 objects with $|g - r| > 3$ mag, 716 have only two to five $g$ observations and none has more than ten. The phase curves in Figure 5 show both mean phase dependence and epoch-to-epoch scatter; fitted $H$ is not a rotationally resolved light curve.

### 5.4. *Other `SSObject` Fields and Usage Considerations*

In addition to the photometric fit outputs, `SSObject` records the total and per-band observation counts, first observation epoch, observing arc, per-band phase-angle limits, and extendedness summaries. Although most objects are point-like, 14,663 (4.9%) have median extendedness of at least 0.5. Its weak correlation with predicted rate means that a high value need not imply trailing; blending and low-signal-to-noise classification can also contribute.

The table also includes the Tisserand parameter with respect to Jupiter and Earth minimum orbit intersection distance (MOID) quantities computed from the input MPC orbital elements. DP2 does not refit object orbits from the Rubin observations. The MOID calculation uses Earth elements evaluated at each object's

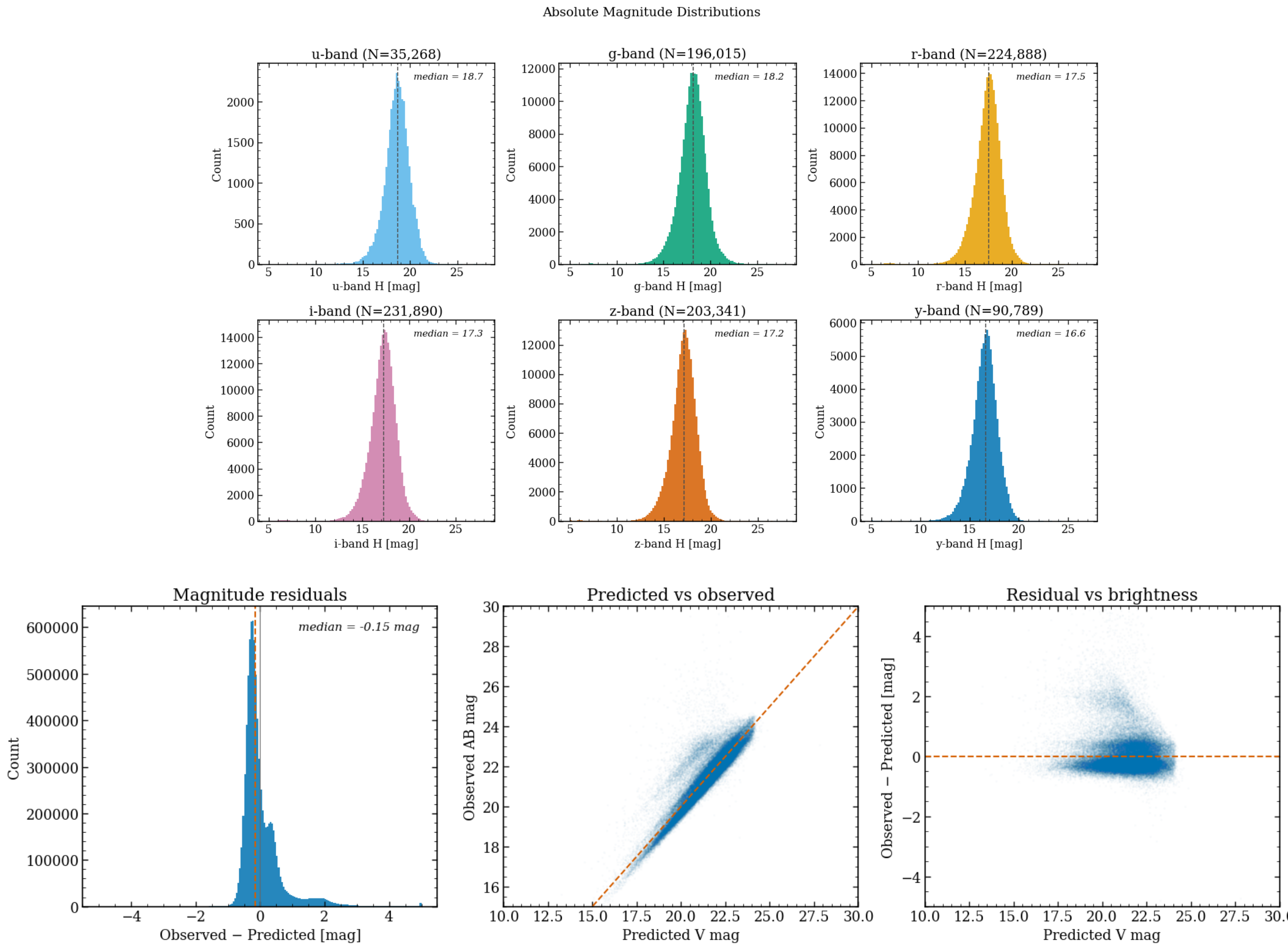


**Figure 4.** Photometric properties of the associations and fitted objects. *Top:* Per-band absolute-magnitude distributions; panel titles give the number of valid fits and dashed lines mark the medians. *Bottom:* Comparison of the measured apparent AB magnitude with the predicted Johnson $V$ magnitude. The left panel shows the observed-minus-predicted distribution, the center panel the direct comparison, and the right panel the residual as a function of predicted brightness. The measured points combine all six Rubin bands, so color terms, phase-model differences, and measurement scatter all contribute; these panels are not a same-band photometric calibration test. The raster panels are taken from the validation notebooks and will be regenerated from the final parquet tables for publication.

osculating epoch. For 67,246 objects with a comparison value in the MPC catalog, the median DP2-minus-MPC difference is approximately 0.1 mau and 65.4% agree within 0.001 au. Discrepancies can reach about 0.003 au among objects with very small MOID, however, and the supplied values should not be used by themselves for hazard classification or close-approach prediction.

For most analyses, `SSObject` is the starting point for cuts on count, arc, phase coverage, and fit quality; join by `ssObjectId` for epoch-level `SSSource` quantities. Residual studies must account for the hard 1″ truncation, and population studies for the input catalog, footprint, cadence, and difference-image detection. These are product selection effects, not properties of the underlying population.

## 6. PERFORMANCE CHARACTERIZATION AND KNOWN ISSUES

## 7. RUBIN SCIENCE PLATFORM

## 8. SUPPORT FOR COMMUNITY SCIENCE

Rubin Observatory's model to support its large, diverse science community to access and analyze DP2 focuses on providing documentation, tutorials, and live virtual learning opportunities alongside an open platform for issue reporting and resolution that enables crowd-sourced solutions. These support resources are all available via the main hub of Rubin's "For Scientists" website[6].

[6] https://rubinobservatory.org/for-scientists

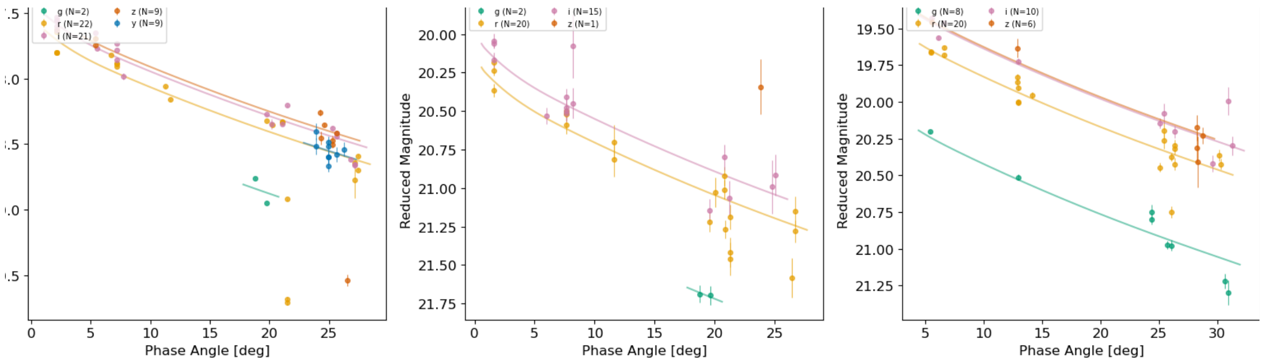


**Figure 5.** Example distance-reduced phase curves for 2001 QD225, 2025 NW98, and 2006 QP137 (left to right), with observations colored by band and the corresponding fixed-$G_{12} = 0.5$ models shown as solid lines. These raster panels are taken from the validation notebooks and will be regenerated from the final parquet tables for publication.

The data release documentation for DP2[7] provides an overview of the LSSTCam observations, data quality summary plots, and descriptions of the contents and access methods for all catalog and image datasets. All tutorials (NSF-DOE Vera C. Rubin Observatory 2021) that demonstrate DP2 access via the Rubin Science Platform are delivered in the data release documentation, and executable versions of the Jupyter notebook tutorials are also available from a drop-down menu within the Notebook Aspect.

Early DP2 was released on the first day of the annual Rubin Community Workshop, July 27 2026. A dedicated "Get started with DP2" session was added to the Wednesday agenda. Four DP2-onboarding virtual sessions were run in the first week of August, a mix of presentations, tutorials, and time for issue resolution.

The Rubin Community Forum[8] is the open platform for user issue reporting and resolution. Rubin staff monitor all new topics posted in the Support category and ensure that all requests for help get a response and a solution. The open nature of the platform also enables peer-to-peer support that avoids knowledge bottlenecks and hastens the time to resolution.

## 9. SUMMARY AND FUTURE RELEASES

DP2 provides the first release of science-grade data products from the LSSTCam focal plane. As for DP1, DP2 is part of Rubin's Early Science Program (Guy et al. 2026) and carries a 2 yr proprietary period during which access is restricted to LSST data rights holders via the cloud-based RSP.

DP2 is delivered in two phases: Early DP2 (EDP2), which provides deep coadded images, all science catalogs, and ancillary data products including throughput curves, survey property maps, and calibration products; and DP2, planned for late 2026, which adds single-epoch visit-level and difference-image data products to complete the release. The coadded images and catalogs delivered in EDP2 will not be reprocessed for DP2; the data are unchanged, and DP2 supersedes and fully encompasses EDP2 by adding the remaining products to the same release. Analyses begun on EDP2 products require no modification.

DP2 represents a substantial advance relative to DP1: the full LSSTCam focal plane replaces the single-raft LSSTComCam, all six *ugrizy* filters are available in place of three, and the sky area is larger by approximately two orders of magnitude. Nevertheless, DP2 reflects the state of an observatory still in the process of optimization: delivered image quality had not yet consistently reached design specification, template coverage is incomplete across the full sky, and several pipeline components remain under active development. Users are encouraged to consult the release documentation at https://dp2.lsst.io and the known issues register maintained there before beginning scientific analyses.

The body of science-grade LSSTCam data acquired between the end of the DP2 observing window on 2026-01-06 and the formal start of the LSST on 2026-06-29 will be processed and made available to LSST data rights holders through the same RSP services. The format and timing of this release are still under discussion; planning will be finalised once DP2 has been delivered.

The first LSST Data Release, Data Release 1 (DR1), will be derived from a reprocessing of approximately the first year of LSST survey data and is currently expected in mid-2028; its precise definition remains under consideration. DR1 will mark a qualitative advance beyond DP2: observations collected under the community-developed baseline survey strategy (Rubin's Survey Cadence Optimization Committee et al. 2022, 2023, 2025; The Rubin Observatory Survey Cadence Optimization Committee 2026) will yield substantially

[7] https://dp2.lsst.io
[8] https://community.lsst.org/

broader and more uniform sky coverage across the full Wide-Fast-Deep (WFD) footprint of 18000 $deg^2$, a balanced six-band filter distribution, and improved delivered image quality as AOS and dome thermal management continue to mature (NSF-DOE Vera C. Rubin Observatory 2026). Photometric and astrometric calibration will benefit from a full year of all-sky coverage, difference-imaging templates will span a far greater fraction of the footprint and processing will draw on a more mature version of the LSST Science Pipelines refined through DP2 experience and community engagement. Subsequent LSST Data Releases are planned at an approximately yearly cadence, each a complete reprocessing of all survey data accumulated to that point, with progressively deeper coadds and improved calibration. Plans will be updated through revisions to Guy et al. (2026) and on the Rubin community forum at https://community.lsst.org.

## ACKNOWLEDGMENTS

. This material is based upon work supported in part by the National Science Foundation through Cooperative Agreements AST-1258333 and AST-2241526 and Cooperative Support Agreements AST-1202910 and AST-2211468 managed by the Association of Universities for Research in Astronomy (AURA), and the Department of Energy under Contract No. DE-AC02-76SF00515 with the SLAC National Accelerator Laboratory managed by Stanford University. Additional Rubin Observatory funding comes from private donations, grants to universities, and in-kind support from LSST-DA Institutional Members.

This work has been supported by the French National Institute of Nuclear and Particle Physics (IN2P3) through dedicated funding provided by the National Center for Scientific Research (CNRS).

This work has been supported by STFC funding for UK participation in LSST, through grant ST/Y00292X/1.

*Facilities:* Rubin:Simonyi (LSSTComCam), Rubin:USDAC

*Software:* Rubin Data Butler (Jenness et al. 2022), LSST Science Pipelines (Rubin Observatory Science Pipelines Developers 2025), LSST Feature Based Scheduler v3.0 (Jones 2026; Yoachim et al. 2024; Naghib et al. 2019), Astropy (Astropy Collaboration et al. 2013, 2018, 2022), PIFF (Jarvis et al. 2021), GBDES (Bernstein 2022), MultiProFit (Taranu 2025), Qserv (Wang et al. 2011; Mueller et al. 2025), Slurm, HTCondor, CVMFS, FTS3, ESNet

## APPENDIX

### Glossary

**AOS:** Active Optics System.

**AURA:** Association of Universities for Research in Astronomy.

**DAC:** Data Access Center.

**Data Management System:** The computing infrastructure, middleware, and applications that process, store, and enable information extraction from the LSST dataset; the DMS will process petascale data volume, convert raw images into a faithful representation of the universe, and archive the results in a useful form. The infrastructure layer consists of the computing, storage, networking hardware, and system software. The middleware layer handles distributed processing, data access, user interface, and system operations services. The applications layer includes the data pipelines and the science data archives' products and services.

**DIA:** Difference Image Analysis.

**DOE:** Department of Energy.

**DP0:** Data Preview 0.

**DP1:** Data Preview 1.

**DP2:** Data Preview 2.

**DR1:** Data Release 1.

**EDP2:** Early Data Preview 2.

**exponential profile:** The radial distribution of flux of an astronomical source that is characterized: I(r)=I0exp(.68(r/re)) The normalization 1.68 is chosen so that the model radius is a half-light radius. An 2-dimensional elliptical version of this profile is fit to every detected source.

**flux:** Shorthand for radiative flux, it is a measure of the transport of radiant energy per unit area per unit time. In astronomy this is usually expressed in cgs units: erg/cm$2$/s.

**footprint:** See 'source footprint', 'instrumental footprint', or 'survey footprint', 'Footprint' is a Python class representing a source footprint.

**GAaP:** Gaussian Aperture and PSF.

**HSM:** Shape measurement algorithm from Hirata & Seljak (2003) and Mandelbaum et al. (2005).

**LSST:** Legacy Survey of Space and Time.

**LSSTCam:** LSST Science Camera.

**LSSTComCam:** Rubin Commissioning Camera.

**MultiProFit:** The MultiProFit astronomical source modelling code, including the multiprofit Python package and its dependencies, and the meas_extensions_multiprofit package for pipeline tasks..

**NSF:** National Science Foundation.

**Object:** In LSST nomenclature this refers to an astronomical object, such as a star, galaxy, or other physical entity. E.g., comets, asteroids are also Objects but typically called a Moving Object or a Solar System Object (SSObject). One of the DRP data products is a table of Objects detected by LSST which can be static, or change brightness or position with time.

**PPDB:** Prompt Products DataBase.

**PSF:** Point Spread Function.

**RSP:** Rubin Science Platform.

**scarlet lite:** The "lite" version of the scarlet algorithm, optimized for multiband deblending on pixel-aligned grids. Includes the scarlet_lite and meas_extensions_scarlet Python packages..

**ShearObject:** An object with measurements using the metadetection algorithm, or the catalog thereof..

**SNR:** Signal to Noise Ratio.

**USDF:** United States Data Facility.

**WFD:** Wide-Fast-Deep.

## REFERENCES


Abazajian, K., Adelman-McCarthy, J. K., Agüeros, M. A., et al. 2004, AJ, 128, 502, doi: 10.1086/421365

Acero-Cuellar, T., Bianco, F. B., Sánchez, B. O., Sako, M., & Bellm, E. C. 2026, Performance of Machine-Learned Reliability Scoring for Image Differencing, Data Management Technical Note DMTN-337, NSF-DOE Vera C. Rubin Observatory. https://dmtn-337.lsst.io/

Aihara, H., AlSayyad, Y., Ando, M., et al. 2019, PASJ, 71, 114, doi: 10.1093/pasj/psz103

—. 2022, PASJ, 74, 247, doi: 10.1093/pasj/psab122

Alard, C., & Lupton, R. H. 1998, ApJ, 503, 325, doi: 10.1086/305984

AlSayyad, Y. 2018, DMTN-080: Coaddition Artifact Rejection and CompareWarp, Tech. rep., NSF-DOE Vera C. Rubin Observatory, doi: 10.71929/RUBIN/2583441

Armstrong, R., Sheldon, E., Huff, E., et al. 2024, arXiv e-prints, arXiv:2407.01771, doi: 10.48550/arXiv.2407.01771

Astier, P., & Regnault, N. 2023, A&A, 670, A118, doi: 10.1051/0004-6361/202245407

Astropy Collaboration, Robitaille, T. P., Tollerud, E. J., et al. 2013, A&A, 558, A33, doi: 10.1051/0004-6361/201322068

Astropy Collaboration, Price-Whelan, A. M., Sipőcz, B. M., et al. 2018, AJ, 156, 123, doi: 10.3847/1538-3881/aabc4f

Astropy Collaboration, Price-Whelan, A. M., Lim, P. L., et al. 2022, ApJ, 935, 167, doi: 10.3847/1538-4357/ac7c74

Berk, A., Anderson, G. P., Bernstein, L. S., et al. 1999, in Society of Photo-Optical Instrumentation Engineers (SPIE) Conference Series, Vol. 3756, Optical Spectroscopic Techniques and Instrumentation for Atmospheric and Space Research III, ed. A. M. Larar, 348–353, doi: 10.1117/12.366388

Bernstein, G. M. 2022, gbdes: DECam instrumental signature fitting and processing programs, Astrophysics Source Code Library, record ascl:2210.011. http://ascl.net/2210.011

Bernstein, G. M., Armstrong, R., Plazas, A. A., et al. 2017, PASP, 129, 074503, doi: 10.1088/1538-3873/aa6c55

Bertin, E. 2011, in Astronomical Society of the Pacific Conference Series, Vol. 442, Astronomical Data Analysis Software and Systems XX, ed. I. N. Evans, A. Accomazzi, D. J. Mink, & A. H. Rots, 435

Bianco, F. B., Ivezić, Ž., Jones, R. L., et al. 2022, ApJS, 258, 1, doi: 10.3847/1538-4365/ac3e72

Blum, R., & the Rubin Operations Team. 2020, Vera C. Rubin Observatory Data Policy, Data Management Operations Controlled Document RDO-013, NSF-DOE Vera C. Rubin Observatory. https://ls.st/RDO-013

Bosch, J., Armstrong, R., Bickerton, S., et al. 2018, PASJ, 70, S5, doi: 10.1093/pasj/psx080

Broughton, A., Utsumi, Y., Plazas Malagón, A. A., et al. 2024, PASP, 136, 045003, doi: 10.1088/1538-3873/ad3aa2

Burke, D. L., Rykoff, E. S., Allam, S., et al. 2018, AJ, 155, 41, doi: 10.3847/1538-3881/aa9f22

Fagrelius, P., & Rykoff, E. S. 2025, Rubin Observatory Baseline Calibration Plan, Commissioning Technical Note SITCOMTN-086, NSF-DOE Vera C. Rubin Observatory, doi: 10.71929/rubin/2583850

Ferguson, P. S., Rykoff, E. S., Carlin, J. L., Saunders, C., & Parejko, J. K. 2025, The Monster: A reference catalog with synthetic ugrizy-band fluxes for the Vera C. Rubin observatory, Data Management Technical Note DMTN-277, NSF-DOE Vera C. Rubin Observatory, doi: 10.71929/rubin/2583688

Fortino, W. F., Bernstein, G. M., Bernardinelli, P. H., et al. 2021, AJ, 162, 106, doi: 10.3847/1538-3881/ac0722

Guy, L. P., AlSayyad, Y., Bechtol, K., et al. 2026, Rubin Observatory Plans for an Early Science Program, Technical Note RTN-011, NSF-DOE Vera C. Rubin Observatory, doi: 10.71929/rubin/2584021

Holman, M. J., Bernardinelli, P. H., Schwamb, M. E., et al. 2025, AJ, 170, 97, doi: 10.3847/1538-3881/ade435

Howard, J., Reil, K., Claver, C., et al. 2018, in Society of Photo-Optical Instrumentation Engineers (SPIE) Conference Series, Vol. 10700, Ground-based and Airborne Telescopes VII, ed. H. K. Marshall & J. Spyromilio, 107003D, doi: 10.1117/12.2312684

Ivezić, Ž., Kahn, S. M., Tyson, J. A., et al. 2019, ApJ, 873, 111, doi: 10.3847/1538-4357/ab042c

Jarvis, M., et al. 2021, Mon. Not. Roy. Astron. Soc., 501, 1282, doi: 10.1093/mnras/staa3679

Jarvis, M., Bernstein, G. M., Amon, A., et al. 2021, MNRAS, 501, 1282, doi: 10.1093/mnras/staa3679

Jenness, T., Bosch, J. F., Salnikov, A., et al. 2022, in Society of Photo-Optical Instrumentation Engineers (SPIE) Conference Series, Vol. 12189, Software and Cyberinfrastructure for Astronomy VII, 1218911, doi: 10.1117/12.2629569

Jones, R. L. 2026, Scheduling the LSST: Commissioning the Rubin Feature Based Scheduler, Simulations Team Technical Note SMTN-020, NSF-DOE Vera C. Rubin Observatory. https://smtn-020.lsst.io/

Jurić, M., Ciardi, D., Dubois-Felsmann, G., & Guy, L. 2019, LSST Science Platform Vision Document, Systems Engineering Controlled Document LSE-319, NSF-DOE Vera C. Rubin Observatory, doi: 10.71929/rubin/2587242

Kannawadi, A. 2025, Consistent galaxy colors with Gaussian-Aperture and PSF photometry, Data Management Technical Note DMTN-190, NSF-DOE Vera C. Rubin Observatory, doi: 10.71929/rubin/2583849

Karpov, S., & Peloton, J. 2022, arXiv e-prints, arXiv:2202.05719, doi: 10.48550/arXiv.2202.05719

Kron, R. G. 1980, ApJS, 43, 305, doi: 10.1086/190669

Kuijken, K. 2008, A&A, 482, 1053, doi: 10.1051/0004-6361:20066601

Léget, P. F., Astier, P., Regnault, N., et al. 2021, A&A, 650, A81, doi: 10.1051/0004-6361/202140463

LSST Dark Energy Science Collaboration (LSST DESC), Abolfathi, B., Alonso, D., et al. 2021, ApJS, 253, 31, doi: 10.3847/1538-4365/abd62c

Melchior, P., Moolekamp, F., Jerdee, M., et al. 2018, Astronomy and Computing, 24, 129, doi: 10.1016/j.ascom.2018.07.001

Merritt, S. R., Fedorets, G., Schwamb, M. E., et al. 2025, AJ, 170, 100, doi: 10.3847/1538-3881/add3ec

Mueller, F., Gaponenko, I., Gates, J., et al. 2025, in Astronomical Society of the Pacific Conference Series, Vol. 538, Astronomical Data Analysis Software and Systems XXXII, ed. S. Gaudet, D. Bohlender, S. Gwyn, A. Hincks, & P. Teuben, 114, doi: 10.26624/XCPI7375

Muinonen, K., Belskaya, I. N., Cellino, A., et al. 2010, Icarus, 209, 542, doi: 10.1016/j.icarus.2010.04.003

Naghib, E., Yoachim, P., Vanderbei, R. J., Connolly, A. J., & Jones, R. L. 2019, AJ, 157, 151, doi: 10.3847/1538-3881/aafece

NSF-DOE Vera C. Rubin Observatory. 2021, Rubin Observatory LSST Tutorials [Computer Software], NSF-DOE Vera C. Rubin Observatory, doi: 10.11578/rubin/dc.20250909.20

—. 2025, Legacy Survey of Space and Time Data Preview 1 [Data set], NSF-DOE Vera C. Rubin Observatory, doi: 10.71929/RUBIN/2570308

—. 2026, Image Quality Improvement Plan, Summit Operations Technical Note SOTN-004, NSF-DOE Vera C. Rubin Observatory. https://sotn-004.lsst.io/

Oke, J. B., & Gunn, J. E. 1983, ApJ, 266, 713, doi: 10.1086/160817

O'Mullane, W., AlSayyad, Y., Chiang, J., et al. 2024, in Society of Photo-Optical Instrumentation Engineers (SPIE) Conference Series, Vol. 13101, Software and Cyberinfrastructure for Astronomy VIII, ed. J. Ibsen & G. Chiozzi, 131012B, doi: 10.1117/12.3018005

Reiss, D. J., & Lupton, R. H. 2016, Implementation of Image Difference Decorrelation, Data Management Technical Note DMTN-021, NSF-DOE Vera C. Rubin Observatory, doi: 10.71929/rubin/2586490

Rubin, V. C., & Ford, Jr., W. K. 1970, ApJ, 159, 379, doi: 10.1086/150317

Rubin, V. C., Ford, Jr., W. K., & Thonnard, N. 1980, ApJ, 238, 471, doi: 10.1086/158003

Rubin Observatory Science Pipelines Developers. 2025, The LSST Science Pipelines Software: Optical Survey Pipeline Reduction and Analysis Environment, Project Science Technical Note PSTN-019, NSF-DOE Vera C. Rubin Observatory, doi: 10.71929/rubin/2570545

Rubin's Survey Cadence Optimization Committee, Bauer, F. E., Brough, S., et al. 2022, Survey Cadence Optimization Committee's Phase 1 Recommendation, Project Science Technical Note PSTN-053, NSF-DOE Vera C. Rubin Observatory, doi: 10.71929/rubin/2584276

Rubin's Survey Cadence Optimization Committee, Bauer, F. E., Bianco, F. B., et al. 2023, Survey Cadence Optimization Committee's Phase 2 Recommendations, Project Science Technical Note PSTN-055, NSF-DOE Vera C. Rubin Observatory, doi: 10.71929/rubin/2585249

Rubin's Survey Cadence Optimization Committee, Bianco, F. B., Jones, R. L., et al. 2025, Survey Cadence Optimization Committee's Phase 3 Recommendations, Project Science Technical Note PSTN-056, NSF-DOE Vera C. Rubin Observatory, doi: 10.71929/rubin/2585402

Saunders, C. 2024, Astrometric Calibration in the LSST Pipeline, Data Management Technical Note DMTN-266, NSF-DOE Vera C. Rubin Observatory, doi: 10.71929/rubin/2583846

—. 2025, Early astrometric residuals characterization of LSSTCam: Atmospheric turbulences and static sensor effect., Data Management Technical Note DMTN-324, NSF-DOE Vera C. Rubin Observatory. https://dmtn-324.lsst.io/

Schutt, T., Jarvis, M., Roodman, A., et al. 2025, The Open Journal of Astrophysics, 8, 26, doi: 10.33232/001c.132299

Sérsic, J. L. 1963, Boletin de la Asociacion Argentina de Astronomia La Plata Argentina, 6, 41

Sersic, J. L. 1968, Atlas de Galaxias Australes (Cordoba, Argentina: Observatorio Astronomico)

Sheldon, E. S., Becker, M. R., MacCrann, N., & Jarvis, M. 2020, ApJ, 902, 138, doi: 10.3847/1538-4357/abb595

SLAC National Accelerator Laboratory, & NSF-DOE Vera C. Rubin Observatory. 2024, LSST Commissioning Camera, SLAC National Accelerator Laboratory (SLAC), Menlo Park, CA (United States), doi: 10.71929/RUBIN/2561361

Stalder, B., Reil, K., Claver, C., et al. 2020, in Society of Photo-Optical Instrumentation Engineers (SPIE) Conference Series, Vol. 11447, Ground-based and Airborne Instrumentation for Astronomy VIII, ed. C. J. Evans, J. J. Bryant, & K. Motohara, 114470L, doi: 10.1117/12.2561132

Stalder, B., Reil, K., Aguilar, C., et al. 2022, in Society of Photo-Optical Instrumentation Engineers (SPIE) Conference Series, Vol. 12184, Ground-based and Airborne Instrumentation for Astronomy IX, ed. C. J. Evans, J. J. Bryant, & K. Motohara, 121840J, doi: 10.1117/12.2630184

Stalder, B., Munoz, F., Aguilar, C., et al. 2024, in Society of Photo-Optical Instrumentation Engineers (SPIE) Conference Series, Vol. 13094, Ground-based and Airborne Telescopes X, ed. H. K. Marshall, J. Spyromilio, & T. Usuda, 1309409, doi: 10.1117/12.3019266

Taranu, D. S. 2025, The MultiProFit astronomical source modelling code, Data Management Technical Note DMTN-312, NSF-DOE Vera C. Rubin Observatory, doi: 10.71929/rubin/2584108

The Rubin Observatory Survey Cadence Optimization Committee. 2026, Survey Cadence Optimization Committee's Survey Start Recommendations, Project Science Technical Note PSTN-057, NSF-DOE Vera C. Rubin Observatory. https://pstn-057.lsst.io/

Vera C. Rubin Observatory Team. 2026, The Vera C. Rubin Observatory Data Preview 1, Technical Note RTN-095, NSF-DOE Vera C. Rubin Observatory, doi: 10.71929/rubin/2570536

Wang, D. L., Monkewitz, S. M., Lim, K.-T., & Becla, J. 2011, in State of the Practice Reports, SC '11 (New York, NY, USA: ACM), 12:1–12:11, doi: 10.1145/2063348.2063364

Yoachim, P., Jones, L., Eric H. Neilsen, J., & Becker, M. R. 2024, lsst/rubin_scheduler: v3.0.0, v3.0.0, Zenodo, doi: 10.5281/zenodo.13985198

Zuntz, J., Sheldon, E., Samuroff, S., et al. 2018, MNRAS, 481, 1149, doi: 10.1093/mnras/sty2219